

Experimental evidence of T_c enhancement above 50 K and diode and paramagnetic-Meissner effects, in Nickelate films on highly reduced $SrTiO_3$

Anna Eyal* and Gad Koren†

Physics Department, Technion, Haifa, 32000, Israel

(Dated: April 9, 2025)

Since the discovery of superconductivity in nickelate thin films in 2019, the quest for enhancing their T_c has been ongoing. Here we provide experimental evidence for T_c enhancement in oxygen deficient films on highly reduced and conducting $SrTiO_3$ substrates. T_c onset of 50-70 K was found in Meissner and transport measurements, which indicates superconductivity in islands or domains in our films, where T_c of zero resistance is obtained at 20-25 K. In addition, we observed a giant paramagnetic-Meissner effect peak at about 48 K, which further supports the existence of a superconductive transition just above it. Furthermore, an asymmetric or nonreciprocal and non-hysteretic superconductive diode effect was observed. The later could be fully polarized, and its polarity could be reversed. In our films we identified the infinite-layer 112 and the perovskite 113 phases, with a variety of oxygen stoichiometries in between.

I. INTRODUCTION

The discovery of superconductivity in nickelate thin films by the Hwang group in 2019 [1] ignited worldwide interest in this new family of materials [2–10]. Given their similarity to cuprates, nickelates were immediately recognized as a potential new platform for high-temperature superconductivity, as discussed in an early review by Norman [2]. Initial studies focused on mapping the phase diagram of these $Nd_{0.8}Sr_{0.2}NiO_2$ (112 phase) films and characterizing their fundamental properties [3]. Soon after, superconductivity was also observed in $Pr_{0.8}Sr_{0.2}NiO_2$ thin films [4], reinforcing the idea that superconductivity could emerge in multiple members of the nickelate family. However, in both this study and in Ref. [1] the films thickness ranged between 5 and 12 nm only. Thicker films of this kind showed no superconductivity in bulk form [5, 6], and raised the question whether the observed superconductivity in thin films of a few nanometers is an interface effect originating in strains or other interactions with the substrate. More recently, fabrication of free-standing superconducting nickelate films was demonstrated, and a maximum T_c of 25 K was found in films on (110) $NdGaO_3$ [11]. Even higher superconducting T_c values above 30 K at ambient pressure were obtained in ultra thin films of $Sm_{1-x-y-z}Eu_xCa_ySr_zNiO_2$ also on $NdGaO_3$ wafers [12]. The highest T_c so far, of approximately 80 K, was found in well oxygenated single crystals of the double-layer nickelate $La_3Ni_2O_7$ (327 phase) under high pressure of tens of GPa [13]. Another study demonstrated bulk superconductivity in the nickelates, where the reduction process in CaH_2 of perovskite $La_{1-x}Ca_xNiO_3$ single crystals yielded the superconducting infinite layer $La_{1-x}Ca_xNiO_{2+\delta}$ phase

[14]. However, this also led to cracking of these superconducting crystals. Very recently, three studies were reported in which an ambient pressure superconducting T_c onset over 40 K was found in the bilayer 327 phase of nickelate films [7, 15, 16]. In these works, an oxidation annealing step in Ozone was employed in order to get the high T_c phase, unlike previous works on nickelate films where a reduction annealing process, generally in CaH_2 , was used. The highest T_c onset in these studies was obtained in strained $La_2PrNi_2O_7$ films with T_c onset of 48 K by Liu et al. [16].

In earlier studies, most films showing signs of superconductivity were prepared in a two-step process, whereby the perovskite films were deposited first, followed by a second step of reduction in CaH_2 . These films, usually with thicknesses of a few to several nm, were comprised of the infinite-layer 112 phase, possibly in close proximity to the substrate, as the carrier of the superconductive currents. In the most recent study of films of the 327 bilayer phase [16], laser deposition was still used but at a much lower fluence on the target and this was followed by Ozone oxidation. In the present study, we followed the earlier two-steps route and prepared the perovskite phase first, like other groups did. But unlike other groups, the reduction in CaH_2 step was carried out under pumping. This led to an effective reduction not only of the films but also of the $SrTiO_3$ (STO) substrate, which became black and highly conductive. After this annealing process, magnetic moment measurements versus temperature showed a T_c onset at about 50 K. Furthermore, resistance versus temperature of our films showed a T_c onset of 60-70 K and T_c offset with zero resistance at 20-25 K. Therefore, the higher T_c indicates superconductivity in islands, where the lower transition to zero resistance superconductivity is due to the weak-links between them becoming superconducting as well.

In this study we also observed two additional effects. One is a highly asymmetric diode effect in the voltage

* anna.eyal@gmail.com

† gkoren@physics.technion.ac.il

<https://phsites.technion.ac.il/gkoren/>

versus current curves (VICs) without an external magnetic field, where under one polarity of the bias current an Ohmic behavior was found, while in the opposite polarity a supercurrent was observed. However, the sign of this effect could be reversed depending on the distance between the contacts used. This kind of diode effect was recently observed by Qi et al. in BSCCO [17], and theoretically investigated by Mori et al. where a sign reversal was found [18]. The other observation we made is of a giant paramagnetic Meissner effect peak (PME, also known as the Wohleben effect [19]), where a positive magnetization peak appears just below the superconducting transition at about 50 K. This might indicate odd-frequency superconductivity [20], the presence of SN or SF junctions in our samples [21] or the development of a giant vortex state [22]. The PME peaks were most prominent under magnetic fields of thousands Oersted normal to the wafer, unlike earlier studies where fields around one Oersted were used [19].

We believe that the main reason for our extraordinary results originates in the combination of highly reduced black STO substrates and the nickelate films. Stand-alone wafers of pure black STO were metallic, highly conductive and had a superconducting transition at T_c of 0.25 K, similarly to optimally doped reduced STO [23]. When short reduction time was used, we identified the superconductive phase by X-ray diffraction (XRD) as due to the infinite-layer $\text{Nd}_{0.8}\text{Sr}_{0.2}\text{NiO}_2$ as other groups have found, but when the reduction time was increased, XRD of our films showed no particular features beyond the almost disappearance of the perovskite phase. It turned out that in this case, our films became polycrystalline, thus decreasing the XRD signals to their noise level. In both type of cases though, signature of T_c above 50 K was observed. High-angle annular dark-field scanning transmission electron microscopy (HAADF-STEM) measurements identified the structure of our films as due to infinite-layer 112 and perovskite 113 phases, with varying oxygen contents between 2 and 3, as others have found [24–26].

II. EXPERIMENTAL

All our Nickelate films were prepared by pulsed laser deposition (PLD) on optically polished Ti-terminated (100) STO wafers of $10 \times 10 \text{ mm}^2$ area, using a ceramic target of $\text{Nd}_{0.8}\text{Sr}_{0.2}\text{NiO}_3$ (NSNO). In our previous work on NSNO in 2021 [27] we used the third harmonic of a Nd-YAG laser with 355 nm wavelength to deposit the films. This did not yield a dominant perovskite phase of the Nickelate films, as the (001) peak of these films was absent or too weak to be seen. We stress that this was not due to limited resolution of our XRD measurements, since in similar manganite films of $\text{Nd}_{2/3}\text{Sr}_{1/3}\text{MnO}_3$, all (00n) peaks were clearly resolved, including the odd-n

ones. In the present study, we used the fourth-harmonic of the Nd-YAG laser with 266 nm wavelength and this yielded the desired perovskite 113 phase with all the (00n) peaks as depicted in Fig. 1 (a)-(c). Apparently, the deeper UV wavelength is necessary for obtaining the perovskite phase in the Nickelates. This is in contrast to $\text{YBa}_2\text{Cu}_3\text{O}_{7-\delta}$ (YBCO) where all the Nd-YAG harmonics yielded a stable perovskite phase [28]. Films of 10, 20, 30 and 80 nm thickness were prepared, at 780°C heater block temperature ($\sim 600^\circ\text{C}$ wafer temperature) and 100 mTorr O_2 flow. The 266 nm laser operated at 3.3 Hz and was focused to $1.5\text{--}2.5 \text{ J/cm}^2$ on the target. After deposition, 10 Torr of oxygen was added and the sample was cooled to room temperature with a dwell of 1 hour at 450°C.

Reduction or annealing of the films was carried out in aluminum foil packets with 0.35 g of CaH_2 powder at about 320°C, for various durations between one and six hours. Highly resistive films were obtained when using closed packets. However, when a small aperture in the packets was made and the annealing was performed under pumping in a chamber with a base pressure of 10^{-7} Torr at 25°C, low resistance films had been produced. During the actual reduction process at 320°C, the pressure in the vacuum chamber rose to about $5\text{--}10 \times 10^{-7}$ Torr, while inside the packet we estimate that a pressure of around 10^{-5} Torr was obtained due to the differential pumping used. Unlike in other studies, under our annealing conditions, the STO wafers also were reduced and became black, metallic, and highly conductive (apparently on the surface). This was also tested on bare STO wafers without the NSNO films, and the resulting black wafers were also superconducting at 0.25 K as found in the literature for optimally reduced STO [23]. The transport and magnetic results on these wafers served as reference or background for the measurements of the films themselves.

Structural properties of our films were determined by standard $\theta - 2\theta$ x-ray diffraction (XRD) measurements, and the morphology of the films by atomic force microscopy (AFM) images. We also used HAADF-STEM measurements to determine the phases involved and their epitaxiality, defects and crystallinity. Transport measurements of our films were carried out using a PPMS Dynacool system of Quantum Design. When high sensitivity was needed, the PPMS electronics was replaced by an external Keithley 2450 source, while still using the Dynacool's cryogenics. The contacts for the 4-probe measurements were made by a wire bonder with Al wires, and these were also overlaid by freshly applied silver paste bands for increasing the contacts area and thereby reducing their resistance by two orders of magnitude. Magnetic measurements were carried out using a Quantum Design MPMS3 SQUID magnetometer. In these measurements, the samples were placed in a straw of 5 mm diameter in a way that

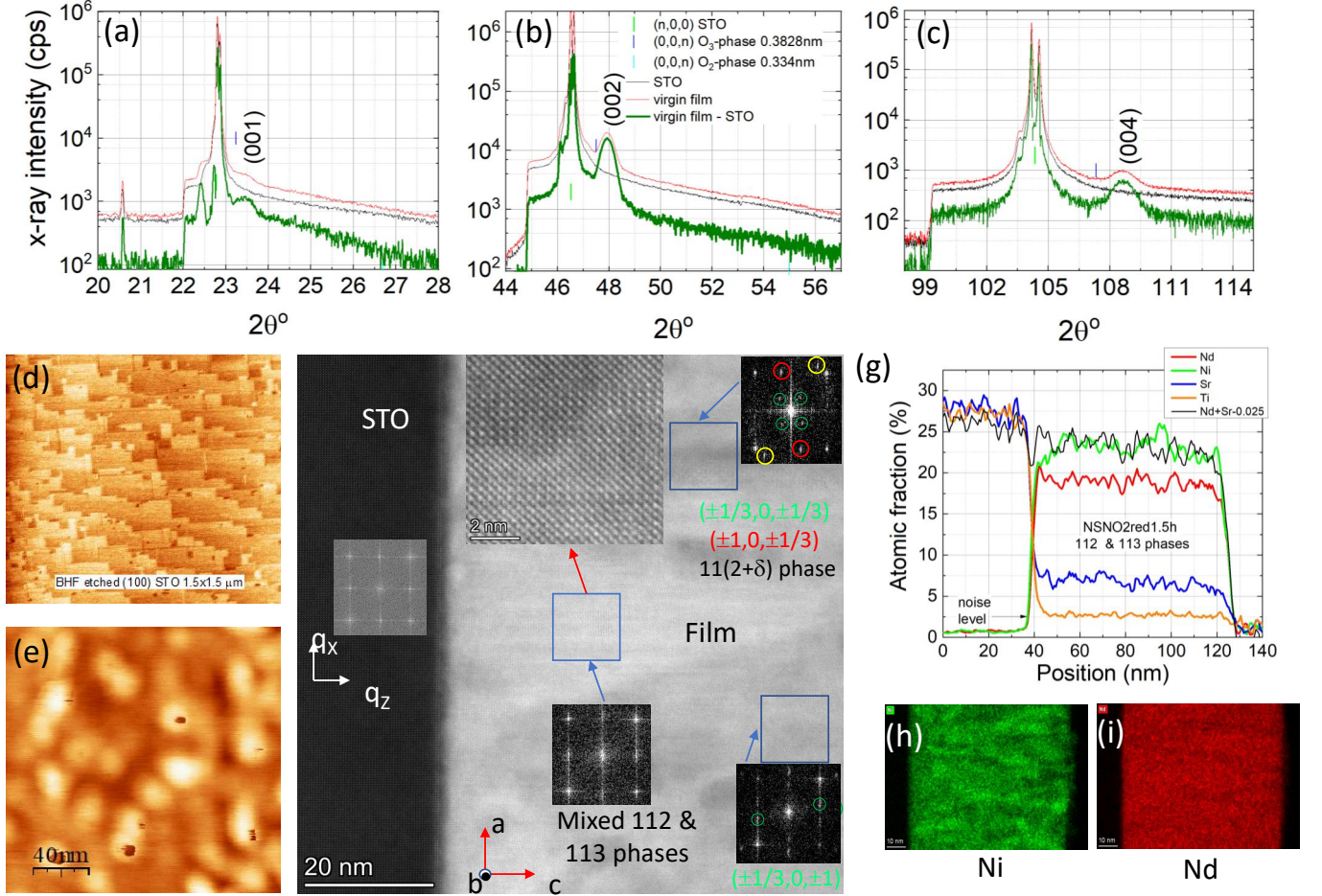


FIG. 1. XRD, AFM and STEM results of 1 and 1.5 h reduced films. (a)-(c) show XRD results of the virgin NSNO1 film, where all the (00n) peaks of the epitaxial $Nd_{0.8}Sr_{0.2}NiO_3$ perovskite phase are seen, except for the weakest (003) peak. (d) shows the surface morphology of a BHF etched and annealed STO wafer with its typical ~ 0.4 nm high unit-cell terraces, on which the NSNO1 film was deposited. (e) depicts the surface morphology of the reduced film NSNO1red1h (reduced in CaH_2 at 320°C for 1 h). (f) shows an HAADF-STEM image of a similarly reduced film NSNO2red1.5h, where the epitaxial film is now quite disordered. FFT on different areas of this film shows variations between infinite-layer 112 and perovskite 113 phases. In particular, the $(\pm 1/3, 0, \pm 1/3)$ (green circled) and $(\pm 1, 0, \pm 1/3)$ (red circled) FFT peaks on the top-right image, indicate intermediate oxygen contents. (g) depicts EDS data of this film where the Nd+Sr atomic fraction is equal to that of the Ni, thus preserving the 112 and/or 113 phases. Also seen in (h) are Ni-rich regions, while in (i) a much more uniform Nd distribution in the film is observed.

the applied magnetic field was perpendicular to the film's surface.

Overall, 12 nickelate films were prepared and characterized in this study using PLD with the fourth-harmonic of the Nd-YAG laser. The virgin films were generally cut into four quarters of $5 \times 5 \text{ mm}^2$ area, for reduction in CaH_2 under different annealing conditions such as temperatures, pressure and time duration. In the present study we report only on the last four films that were reduced in CaH_2 at 320°C and under pumping at local pressure (in the Al packet) of about 10^{-5} Torr. We note here that the AFM images were taken on virgin or pristinely reduced films immediately after their preparation, while the HAADF-STEM results were

obtained on 4 months old films, either after being kept dry in a desiccator or after extensive transport and magnetic measurements.

III. RESULTS

A. Short reduction time film

We start by presenting the morphological and structural characteristics of our films. Figure 1 (d) shows the surface morphology of a BHF etched and $1000^\circ\text{C}/4\text{h}$ annealed STO substrate with terraces of one unit-cell height. The surface morphology of a 30

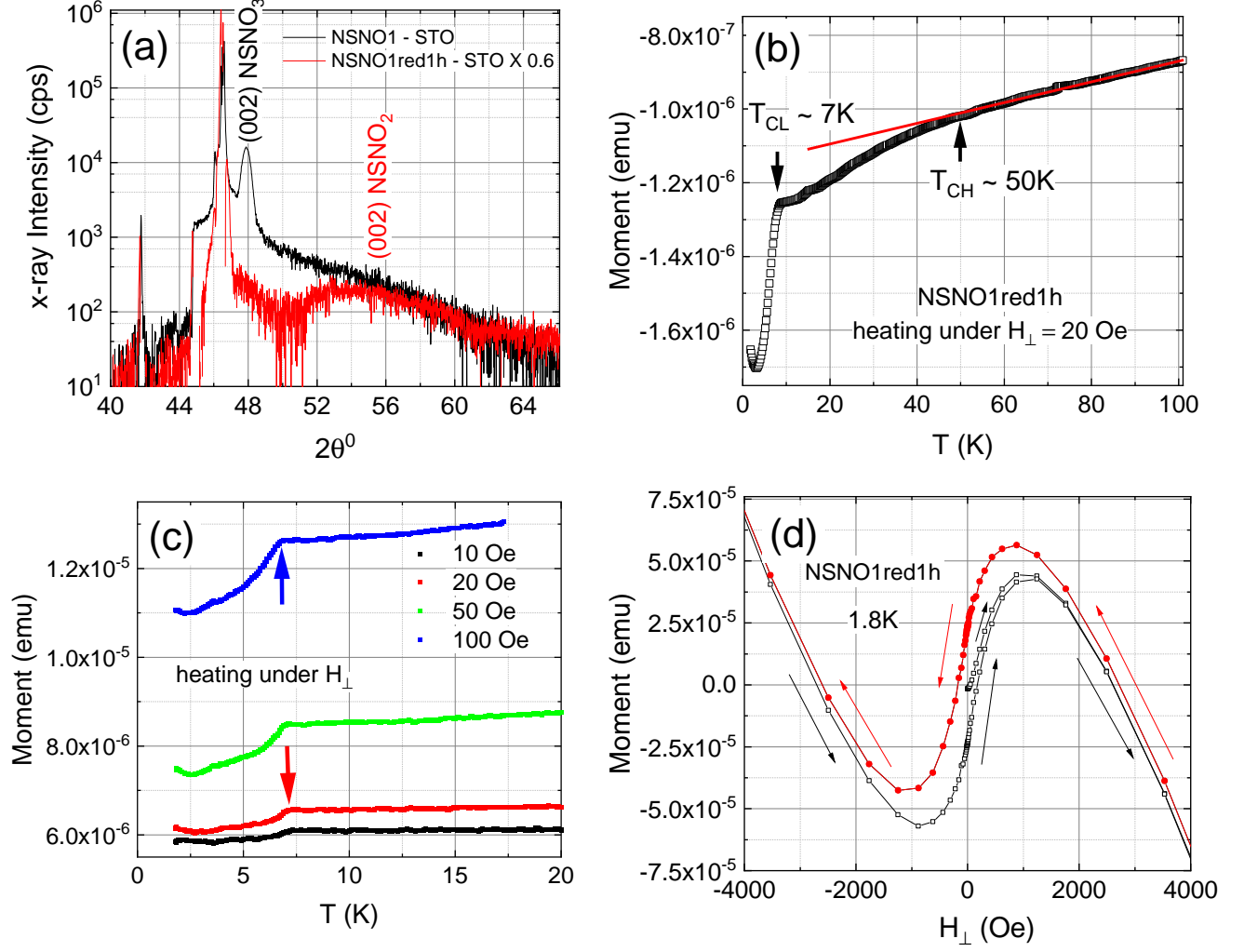


FIG. 2. XRD and magnetization results of NSNO1 and NSNO1red1h films. XRD of the virgin NSNO1 and reduced NSNO1red1h films are shown in (a), where after annealing the prominent perovskite (002) peak of NSNO1 disappears and the broad (002) peak of the infinite-layer $Nd_{0.8}Sr_{0.2}NiO_2$ phase appears. (b) and (c) show magnetic moments versus temperature of NSNO1red1h where two superconducting transitions are observed at about 7 and 50 K in (b), while in (c), scaling of the moment magnitude with field is demonstrated. (d) depicts a magnetic hysteresis loop of this film at 1.8 K after ZFC, where the field was cycled to ± 5000 Oe and back to 0 Oe. The same response as in (d) is obtained also on a bare STO wafer (see Fig. S2 in the supplement).

nm thick NSNO1red1h film grown on it and reduced for 1 h in CaH_2 at 320°C is shown in (e). In (f) we present an HAADF-STEM image of an 80 nm thick film NSNO2red1.5h that was reduced under similar conditions but for 1.5 h. One can see that the reduction process introduced many defects in the virgin epitaxial film. Figure 1 (g)-(i) show the corresponding EDS results of the atomic fractions of the elements in this film and their distribution maps. Clearly, the atomic fraction ratio of $(\text{Nd}+\text{Sr})/\text{Ni}$ is about 1, thus indicating that the $11(2+\delta)$ phase where $0 < \delta < 1$ is preserved. To identify the specific phase in different regions of the film we took their FFT as shown in (f). In the

more ordered region (the whitish triangle in the center of this image) one observes elongation of the FFT quadro pattern along the q_x direction and we found $q_z/q_x \sim 0.95$ as compared to 0.9 found by Rossi et al. in the infinite-layer 112 phase [24]. Thus we have a mixture of 112 and 113 phases in this region. In other regions, the FFT showed peaks at $(\pm 1/3, 0, \pm 1/3)$ (green circled) and $(\pm 1, 0, \pm 1/3)$ (red circled) in the top right image and $(\pm 1/3, 0, 1)$ in the bottom right image. These observations indicate intermediate oxygen content such as in $(Nd_{0.8}Sr_{0.2})_3Ni_3O_7$ which is a $11(2+\delta)$ phase with $\delta=1/3$. We note that this extra oxygen could have been absorbed by the 112 film while kept in a desiccator for 4

months before the STEM measurements were performed.

Next we present XRD data and the magnetic properties of our 1 h reduced film. Figure 2 (a) shows XRD results of a virgin 30 nm thick NSNO1 film together with this film after reduction in CaH_2 at 320°C for 1 h to produce NSNO1red1h. One can see that the perovskite (002) peak of the virgin film disappeared in the reduced film, while a broad (002) peak of the infinite-layer $\text{Nd}_{0.8}\text{Sr}_{0.2}\text{NiO}_2$ phase appeared. We stress that no other clear film's peaks were observed in the $10^\circ < 2\theta < 140^\circ$ range of this XRD spectrum. Since the film is quite disordered as can be seen in a similar film in Fig. 1 (f), its other peaks could be embedded in the noise level of our x-ray system. The magnetic moment as a function of temperature of the reduced film is shown in Fig. 2 (b), where a zero field cooling (ZFC) to 1.8 K was performed, followed by applying a magnetic field of 20 Oe and measuring the moment while heating the sample, as in standard Meissner effect measurement.

Two superconducting transitions are seen in Fig. 2 (b). A sharp one with T_c onset at about 7 K, and a more moderate one with T_c onset at about 50 K. Figure 2 (c) depicts the moments versus temperature at a few low fields, showing that their magnitude is proportional to the fields used, and also that the transition onset temperature is slightly suppressed with increasing field. We point out that the moments in Fig. 2 (b) are negative while in Fig. 2 (c) they are positive. This seemingly

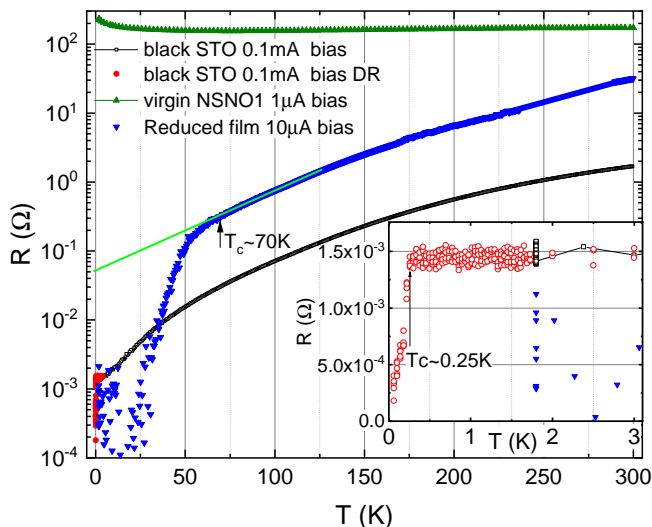


FIG. 3. Resistance versus temperature of the virgin NSNO1 and reduced NSNO1red1h films, together with the R vs T of a bare black STO wafer (reduced in CaH_2 at 320°C for 6 h). In the inset, a zoom-in on the R vs T data of the main panel below 3 K is shown, where the red circles represent measurements obtained in a dilution refrigerator (DR). The transition to superconductivity at ~ 0.25 K is due to the highly reduced, optimally doped, black STO wafer.

puzzling result is due to the magnetic history of the film and substrate preceding the measurements of the moments. The hysteretic moments versus field of Fig. 2 (d) clearly explains this behavior, as a previous history of high negative fields (-5000 Oe here) will yield negative moments at low fields and vice versa. The hysteresis in this figure also suggests the existence of ferromagnetism in the STO substrate with a saturation field of about 800 Oe. This was established by measuring a bare STO wafer (without a film), where results similar to Fig. 2 (d) were found (see Fig. S2 in the supplement).

We now turn to the transport results of this film before and after annealing for 1 h in CaH_2 . Figure 3 shows the corresponding resistance versus temperature of these films, together with a typical background result of a bare black STO wafer also annealed in CaH_2 but for 6 h. The normal resistance at 100 K is $\sim 1 \Omega$ in the reduced film and that of the black STO is about an order of magnitude lower. However, we can't calculate the resistivity of our films since both film and substrate are conducting, we don't know how thick the conducting layer in the STO is, and we actually have a bilayer with interactions between the layers. Therefore, comparison with ρ values obtained in previous studies can't be made. A transition T_c of about 70 K is clearly seen in the CaH_2 annealed film, with crossing of the black STO curve at ~ 35 K and a drop of more than two orders of magnitude in the resistance down to the noise level below 1 mΩ at about 25 K. This indicates conduction between superconductive islands below 70 K via inter-islands weak-links, which become superconductive at T_c offset of 25 K. We believe this is the highest T_c onset reported at ambient pressure in reduced Nickelate films and that it originates in the infinite-layer 112 phase and its $11(2 + \delta)$ variant with $\delta = 1/3$ as seen in Fig. 1 (f). Figure 3 also shows that besides the fact that the normal black STO resistance is about an order of magnitude lower than that of the Nickelate film, this STO has a superconducting transition T_c at 0.25 K as depicted in the inset to this figure. This is typical of oxygen deficient, optimally reduced STO as reported in the literature [23].

B. Longer reduction time film

The strikingly high T_c values observed in our reduced film at ambient pressure, compelled us to double check these results and repeat the experiments on a second freshly prepared film. The laser fluence on the target this time was higher than in the original NSNO1 film (2.5 versus 1.5 J/cm^2), resulting in a much thicker film. Figure 4 (a) and (b) depict two AFM images of this 80 nm thick film, where the surface morphology of the virgin film NSNO2 is seen in (a), and that of the reduced film NSNO2red6h in (b) (reduced in CaH_2

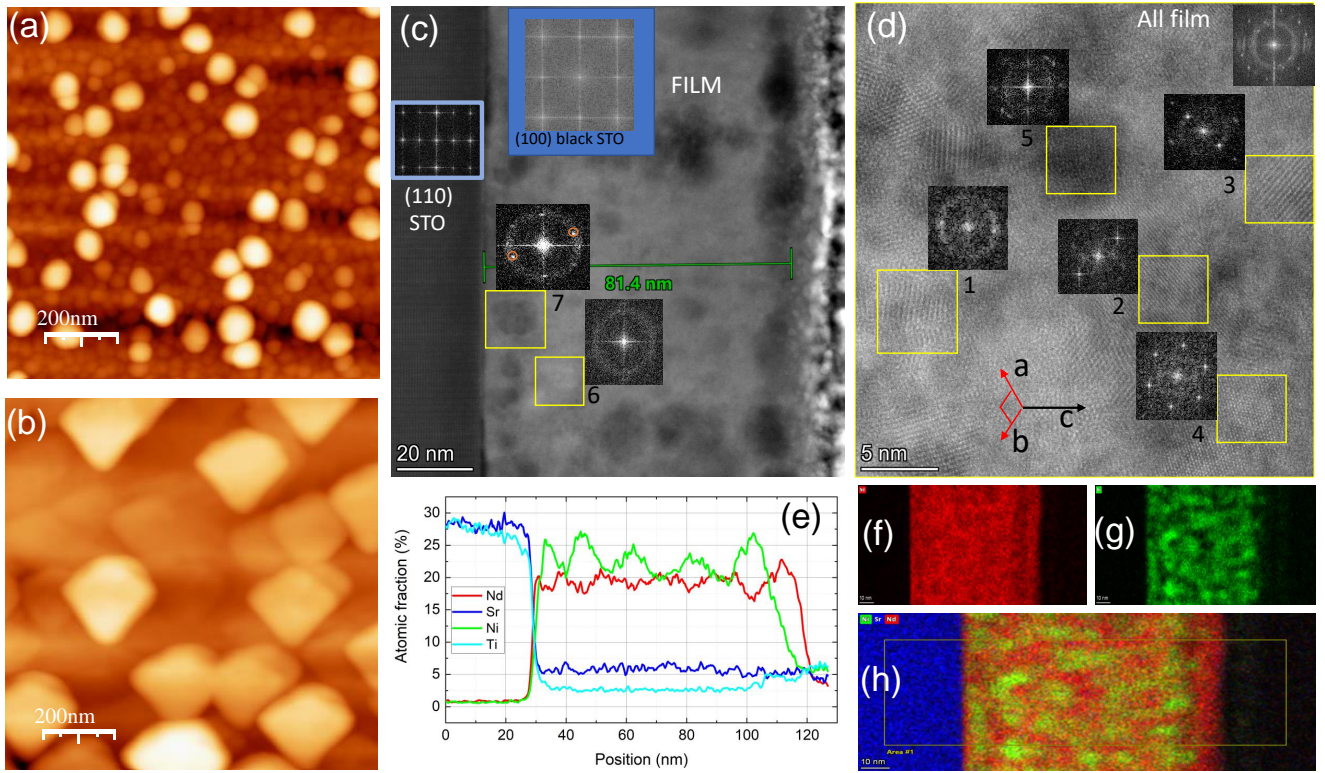


FIG. 4. AFM and STEM results of the 80 nm thick virgin NSNO2 and reduced NSNO2red6h films. (a) and (b) show AFM images of the surface morphology of the NSNO2 and NSNO2red6h films, respectively. (c) and (d) depict STEM images of this 6 h reduced film, where it became polycrystalline. FFT on different areas of this film show stripes normal to the STO main axes as seen in regions 1, 2 and 3 in (d), but overall the film diffraction yields rings like one gets from a powder sample. Two strong $((1/3\sqrt{2}, 1/3\sqrt{2}, 1)$ diffraction peaks are observed on darker areas of the film as in region 7 of (c), indicating oxygen off stoichiometry of the 112 phase such as in $(Nd_{0.8}Sr_{0.2})_3Ni_3O_7$ $11(2+\delta)$ phase with $\delta = 1/3$). (e) depicts EDS data of this film where the Nd+Sr atomic fraction is equal to that of the Ni, except for the top damaged surface layer which is Nd-rich. Thus, as in the more ordered film of Fig. 1, the 112 and/or 113 phases are present. (f-h) show atomic distribution maps of the elements in this film, but now the Ni distribution in the film is even less uniform than that seen in Fig. 1. The overall ratio of the $(Nd+Sr)/Ni$ atomic fraction is still around 1, but the fluctuations are about twice as large as in Fig. 1 (about 10 vs 5%).

at 320°C for 6 h). One can see many particulates and out-growths of 10-25 nm height on the virgin film, and good crystallization at the background with grain sizes of about 50 nm. The reduced film shows a remarkable crystallization, where the particulate in (a) decreased in height to about 10 nm, developed a clear rectangular shapes along the (110) direction, and had background grain sizes of ~ 100 nm.

HAADF-STEM images of the 4 months old NSNO2red6h film after its transport and magnetic measurements are shown in Fig. 4 (c) and (d), together with FFT images of specific regions of this film. The TEM lamella was prepared by FIB lift-off along the (110) direction of the STO wafer as also observed by its corresponding FFT in (c). Also shown in (c) is the FFT of (100) STO for comparison. The c-axis in (d) is in the image plane, while the a and b axes are in a plane normal to the image and at 45° to it. One can see that this film is very disordered and polycrystalline

as indicated by the rings observed in most FFT images in (c) and (d), like in powder diffraction. Nevertheless, some areas of the film show stripes normal to the main axes of the STO wafer as depicted by regions 1, 2 and 3 in Fig. 4 (d), as well as the hexagon in the (111) direction as seen in area 4. In addition, in specific darker areas in (c), as in region 7, prominent $(1/3\sqrt{2}, 1/3\sqrt{2}, 1)$ FFT peaks were observed, similar to the $(1/3, 0, 1)$ peaks in Fig. 1 (f) (note the different axes orientations in these two Figures). This indicates that the $11(2+\delta)$ phase with $\delta = 1/3$ is present also here in the NSNO2red6h film.

Magnetization measurements versus temperature of the oxygen deficient sample are shown in Fig. 5 (a), (b) and (c). In this set of measurements, the standard Meissner procedure of zero field cooling, followed by applying the field at 1.8 K and measuring the moments while heating, was followed by an oscillative field zeroing at 300 K, to ensure that the field was actually close to zero in the next ZFC (and for the initial cooldown, even

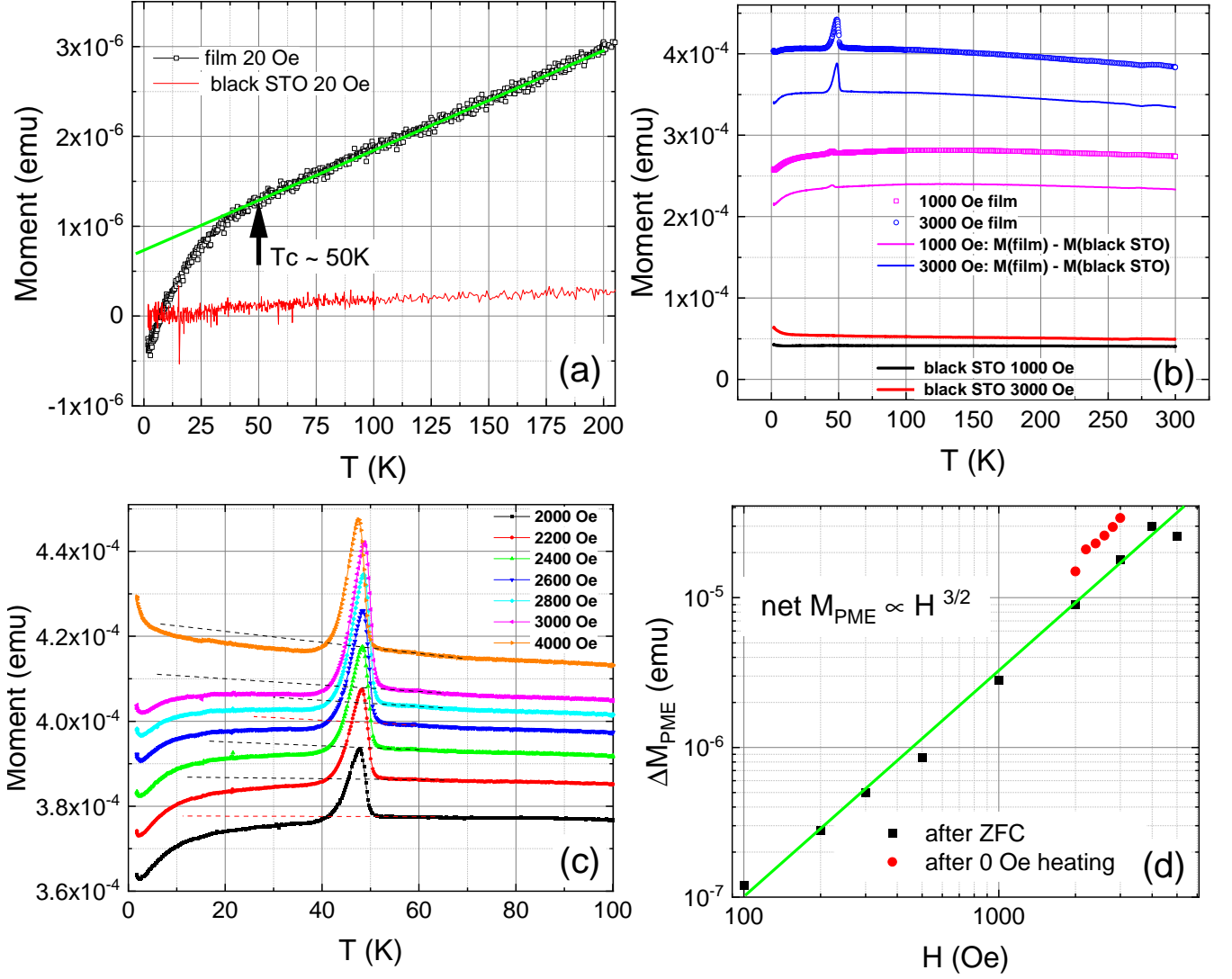


FIG. 5. Magnetic moment results. (a) shows the Meissner moment versus temperature of the NSNO2red6h film and of a bare black STO wafer under the same reduction conditions. The latter represents the small background contribution of the substrate to the moment of the film. The moments of this film and its bare substrate are depicted in (b) under 1000 and 3000 Oe, together with the net moments of the film after subtraction of the substrate contribution. (c) shows consecutive moment measurement results versus temperature and under different fields, where the paramagnetic Meissner effect (PME) peak is robust. In (d) we plot the net PME peak magnitude versus field, where the line represents a power-law behavior with exponent of $3/2$.

less than 0.02 Oe). As can be seen in (a), a Meissner effect is apparent, above a small magnetic background from the STO substrate. The transition again isn't sharp, yet it is clear that the transition temperature is at about 50 K. In Fig. 5 (b) moment results are shown for two higher fields with their corresponding black STO background. Also shown are the net film signals after subtraction of their STO backgrounds. We note that this time, both film and bare STO wafer went through the same 6 h annealing in CaH_2 . The new feature observed under these fields is an emerging positive peak just below 50 K. This peak can be attributed to the paramagnetic Meissner effect (PME), which generally appears just

below the superconducting transition temperature [19].

The appearance of the PME can be explained theoretically as due to the presence of an odd-frequency order parameter, the existence of SN or SF junctions in our films, or a giant vortex state in them [20–22]. Junctions are quite obviously present in our films, as depicted in the schematic diagram of the inset to Fig. 6. This will be elaborated on in more details in the discussion section. More systematic measurements were carried out under fields of 2000 to 4000 Oe as shown in Fig. 5 (c), where the giant PME peaks are clearly larger than the magnitude of the whole Meissner effect drop with

decreasing temperature. We note that the magnitude of these Meissner drops decreases with increasing field, and disappears at 4000 Oe, though the moment at temperatures above the PME peaks are always higher than just below it (see the dashed lines). The main point though of the observation of a giant PME at ~ 48 K in our films, is to further support the existence of superconductivity with T_c slightly above it at 50 K. In Fig. 5 (d) we plot on a lg-lg scale the net PME peak magnitude versus field and find a power law behavior with an exponent of $3/2$. We know of no theory to explain this behavior at the present time.

Transport results of R versus T of NSNO2red6h are shown in Fig. 6 together with the black STO background (times 10). T_c onset here is again at 70 K as in NSNO1red1h of Fig. 3, but the transition to superconductivity doesn't go to zero and ends with a finite resistance at 1.8 K. This however, is an artifact produced by the PPMS measuring system, since in the low temperature regime below ~ 20 K, the voltage versus current curves at low bias are very asymmetric as can be seen in Fig. 7. Actually, they show a clear diode effect which will be discussed later on. Here we shall only point out that the PPMS system calculates the low bias resistance from both the resistive and superconductive parts of these curves, thus yielding a misleading finite resistance result. If one takes only the flat superconductive part of the V vs I curves of Fig. 7, one gets supercurrents and the resistance drops to its noise level. R calculated from such VICs are plotted by the red circles in Fig. 6. This shows a near-coincidence with the PPMS results above 25 K, with a sharp drop below it. Comparing the results of Fig. 6 and Fig. 3, one sees that the R drop in Fig. 3 is more moderate but it starts already at 50 K. Nevertheless, in both cases the R values drop to the noise level at about ~ 20 K and ~ 25 K, respectively. We thus conclude that the basic Meissner and T_c properties of both NSNO1red1h and NSNO2red6h films are quite similar. The differences in the observation of the giant PME peak and asymmetric diode effect in NSNO2red6h might be attributed to the longer annealing duration of this film. In the supplement in sections C and D, we present data of two more films we measured, of 10 and 20 nm thickness, with varying annealing times, that support the $T_c > 50$ K enhancement result here.

Next we present the diode effect and supercurrent results of NSNO2red6h as shown in Figs. 7 and 8. We start with Fig. 7 (a) and (b) where the ramping up of the current is separated from the ramping down by their respective colors (black and green). One can see that the V vs I curves here have two typical kinds of noise. The standard voltage noise with peak to peak amplitude of about $5 \mu\text{V}$, and a telegraph noise jumps of about $7 \mu\text{V}$. These noises are almost averaged out to about $12 \mu\text{V}$ when sampling on a larger number of

points (2000 vs 1000 points in (b) and (a), respectively). A remarkable feature in Fig. 7 is the observation of highly asymmetric curves which indicates a clear diode effect. We extract the supercurrents from the flat horizontal parts of these curves as depicted by the blue lines in Fig. 7. For instance, at 12 K in (c) one can see a small flat part with still asymmetric resistances on both its sides. This resistance asymmetry is almost gone at 20 K as seen in (d). We note that the whole V vs I curves here are shifted to small positive voltages. The shift is 0.35 mV at 1.8 K, while with increasing temperature it decreases to 0.22 mV at 20 K. This voltage shift behavior vs temperature can be better seen in the current vs voltage curves in Fig. 8 (c), where at 50 K it completely disappears. These voltage shifts are unclear to us at the present time, but they could arise from thermo-electric effects between the voltage contacts.

Figure 8 presents the more standard current versus voltage curves (IVCs) and the supercurrents versus temperature. The main differences between Fig. 7 and Fig. 8 are that the former represents raw data measured with one week old Ag-paste contacts, while the later shows smoothed data measured on freshly prepared Ag-paste contacts. Fig. 8 (a) and (b) show how the $\pm 2.5 \mu\text{V}$ criterion to determine the critical current was used (see the shaded rectangles). It also shows that while in

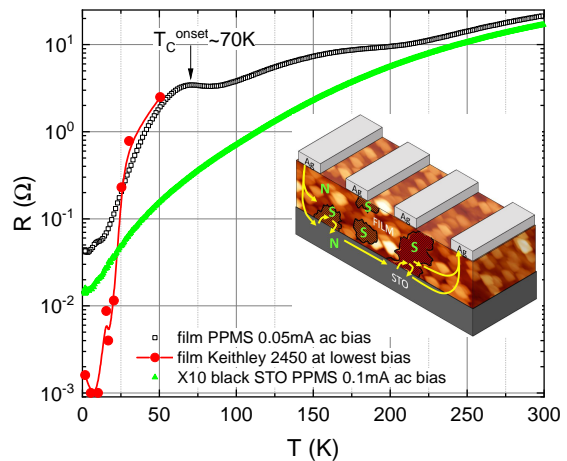


FIG. 6. Resistance versus temperature of the reduced NSNO2red6h film (black squares), together with the R vs T of a bare black STO wafer times 10 (green triangles), both measured using the PPMS system and its software. The red dots represent resistance values measured from the low bias IVCs by a Keithley 2450 source-meter, by taking into account only the minimal resistance parts of the IVCs and avoiding the resistance parts due to the diode effect (below about 20 K). The inset shows a schematic drawing of the sample, bias current flow directions and the contacts geometry, where the shaded areas represent the superconducting islands (S).

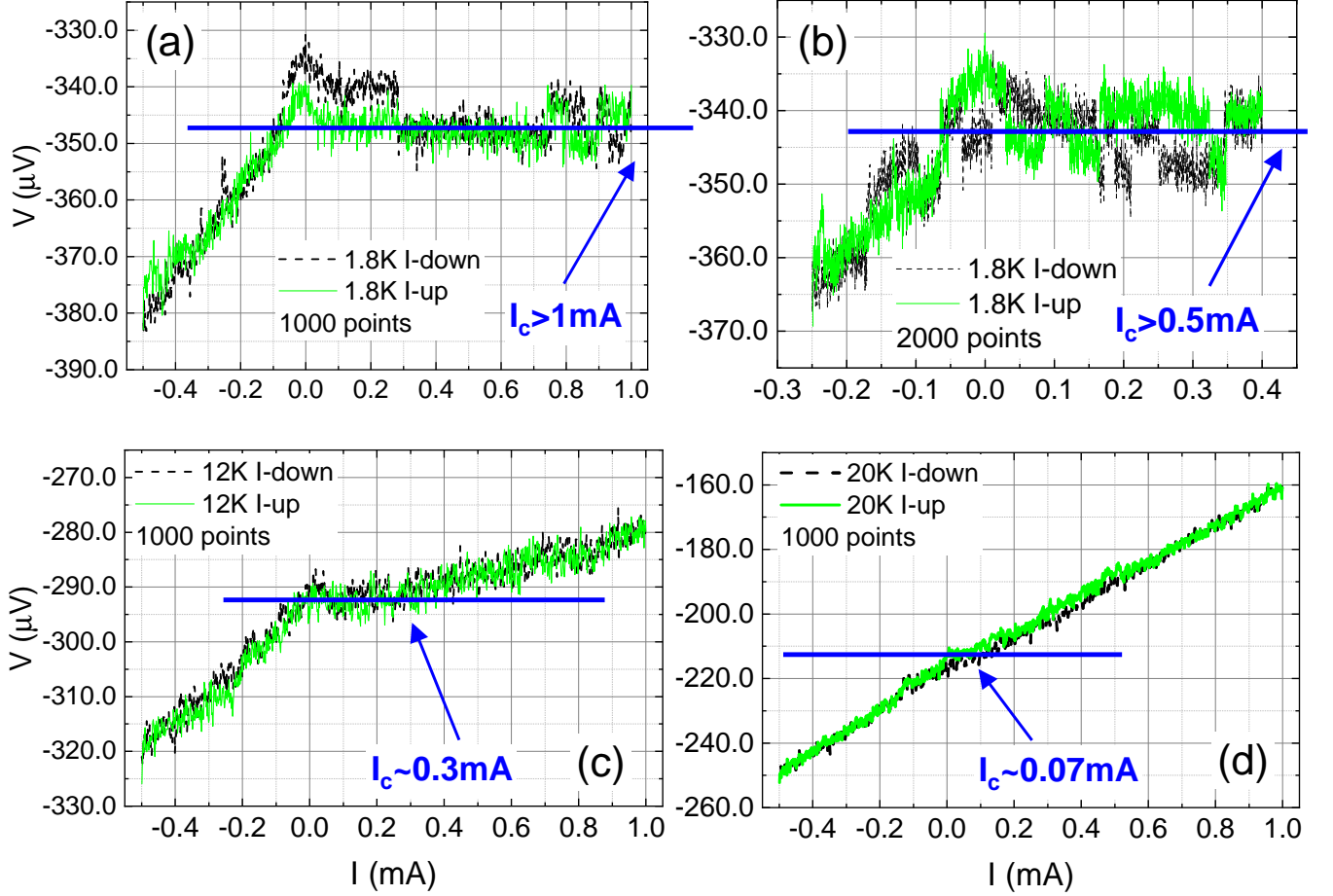


FIG. 7. Voltage versus current curves of NSNO2red6h with one week aged Ag contacts as appeared on the monitor of the Keithley 2450. No averaging was used in these measurements. (a) and (b) were taken at 1.8 K, (c) at 12 K and (d) at 20 K. Up-current scans are plotted in green, while down-current scans are plotted in black. Running voltage noise level at 1.8 K is about $5 \mu\text{V}$ and telegraph noise jumps are of about $7 \mu\text{V}$.

(b) the diode effect is fully asymmetric (resistance starts immediately above zero bias), in (a) the asymmetry shows both positive and negative supercurrents (I_c^+ and I_c^- , respectively). In Fig. 8 (c), a few IVCs are plotted, and the resulting combined supercurrents $I_c^+ + |I_c^-|$ as extracted from these and more IVCs are given versus temperature in (d). We note that below about 5 K, $I_c^+ + |I_c^-|$ in Fig. 8 (d) should actually be higher than 1 mA as can be deduced from Fig. 7 (a) which was obtained with different contacts and without averaging.

IV. DISCUSSION

In the present study, experimental evidence for three novel phenomena in nickelate films was found. T_c enhancement to 50-70 K at ambient pressure, a giant paramagnetic Meissner effect peak around 48 K, and a polarity-reversible diode effect. To the best of our knowl-

edge, T_c above 50 K as found here is the highest reported in reduced nickelate films. Since this effect seems to be strongly dependent on the highly reduced STO substrate, we decided to repeat the experiment on a different new film but with a longer annealing time. The high T_c observed was well reproduced in this new film, but in addition giant PME peak and diode effects were discovered. In the following, we discuss these three phenomena.

A. T_c enhancement

Ever since the discovery of superconductivity in reduced nickelate thin films [1], the quest to increase their T_c has been ongoing. By better controlling the deposition, composition and annealing in CaH_2 conditions, success was achieved but it seems the substrate on which the films were deposited, played a major role in obtaining the highest T_c value. Instead of the commonly used STO substrate, the use of NdGaO_3 substrates

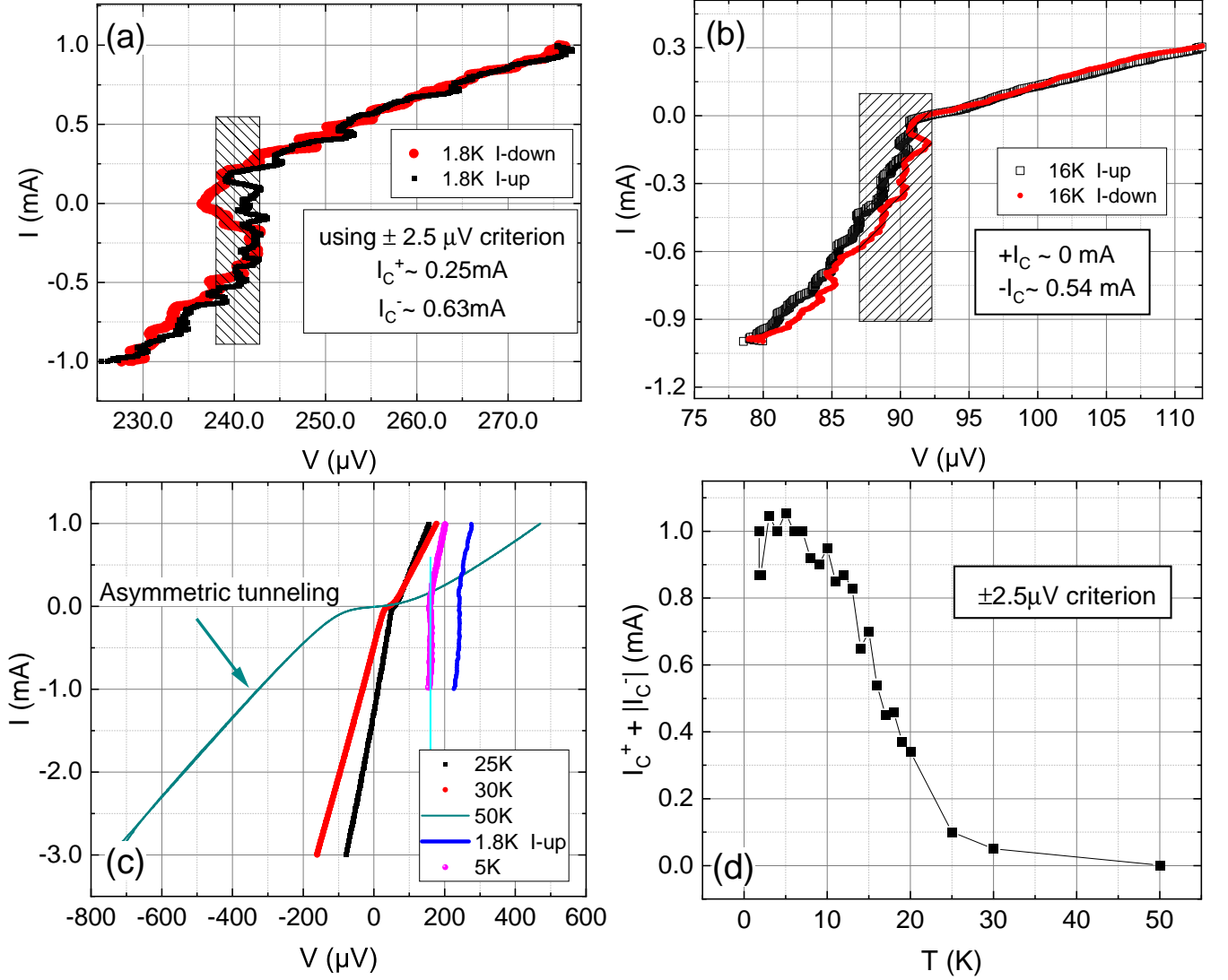


FIG. 8. Current versus voltage curves (IVCs) of the NSNO2red6h film are depicted in (a)-(c) at different temperatures, showing the asymmetric diode effect. Note the reversed polarity at low bias of these curves (more resistive at positive bias) as compared to that of Fig. 7 (more resistive at negative bias). The width of the shaded boxes in (a) and (b) represent the $\pm 2.5 \mu\text{V}$ criterion we used to determine the critical currents which are plotted in (d) versus temperature. Note that the S-shaped band near zero bias of the red curve in (a) is due to averaging over a telegraph-noise jump which isn't included in our voltage criterion (see text). (c) shows that at 50 K there is no I_c and the IVC is still asymmetric and clearly tunneling-like. It also shows the decrease with temperature of the small voltage shift from zero at zero bias.

yielded the highest T_c values so far (25 and 38 K) [11, 12]. In our study, we still use the STO substrate, but in a highly reduced and conducting state and this seems to be the essential ingredient in pushing T_c up. The lattice constant of reduced and normal STO are almost the same [29], therefore the increased T_c doesn't originate in strains in our case. This conclusion is also strengthened by the fact that the present films in which T_c was enhanced are 30-80 nm thick, too thick to be affected by strain with the substrate, unless this is an interface effect. The later is actually the case, as can be deduced from the results in Figs. S3 and S4 of the

supplement, obtained in 20 and 10 nm thick films.

If in fact, the film's layers in close proximity with the substrate are responsible for the elevated T_c observed, then the top layers of the film serve to protect the bottom layers from ambient effects, and the reduced substrate serves as an effective oxygen getter, keeping the film well reduced over time. We noticed aging effects of our films in which over a few months became very resistive, and the STO substrates lost their blackness and returned to their normal whitish transparent color. This obviously originated in the reduced STO absorbing

oxygen from the air, indicating its strong efficiency as a getter even at room temperature.

The STEM and EDS results of Figs. 1 and 4 verify that the main phase involved in the elevated T_c in the present study is still the infinite-layer phase with equal [Nd+Sr] and [Ni] concentrations. But this comes with a modification that the oxygen content can vary between 2 and 3 as found by others [24–26]. The XRD in Fig. 2 (a) points to the presence of the infinite-layer nickelate phase, that was reported already in the pioneering study in which superconductivity in the nickelates was first observed [1]. Figure 2 (b) clearly shows that we have two Meissner transition temperatures in NSNO1red1h which was reduced for 1 h. The fact that in Fig. 5 (a) where the low T_c transition at 7 K is absent, is due to the 6 h long annealing of NSNO2red6h, since in another quarter of the NSNO2 film reduced for 1.5 h to produce NSNO2red1.5h, the 7 K transition was clearly seen (not shown). The XRD of NSNO2red6h film showed no film peaks besides a small remanence "knee" of the (002) peak of the perovskite phase. This is explained in section A and Fig. S1 of the supplement.

B. Meissner and PME effects

Observation of the Meissner effect is a clear signature of superconductivity. It can be seen here in Fig. 2 (b) and Fig. 5 (a) where zero field cooling was followed by heating under 20 Oe. The former shows the low temperature superconducting transition of the $Nd_{0.8}Sr_{0.2}NiO_2$ infinite-layer phase with $T_c \sim 7$ K, together with the $T_c \sim 50$ K transition. This was obtained in a film that was reduced in CaH_2 for 1 h only. When the reduction time was increased to 6 h on a different film as in Fig. 5, the low-temperature transition disappeared and only the high-temperature one persisted. This result could originate in the higher disorder of the longer annealed film as seen in the STEM images of Fig. 4 (c) and (d). Further support for the notion that the $T_c \sim 50$ K transition originates in superconductivity, is given in Fig. 5 (c) where a giant paramagnetic Meissner effect peak appears at ~ 48 K. Such a peak signifies the presence of superconductivity with a transition temperature slightly above it.

The PME peak can be attributed to odd-frequency order parameter which breaks inversion and time reversal symmetries [20]. It could also originate in SN or SF junctions in our film [21], or develop from the formation of a giant vortex state in them [22]. We can not comment on the order parameter symmetry in our films, since we do not have scanning tunneling conductance spectroscopy results on them. It would be interesting to have such data, to prove or refute the odd-frequency nature of the order parameter. The presence of NS or NF junctions in our films is easier to envision from

the inset to Fig. 6, where such junctions form at the interface of the superconducting islands and the STO wafer, or between the islands themselves. The vortex state scenario in our films is quite possible, in particular since the robust PME peaks are observed at quite high fields (2000-4000 Oe). Non-equilibrium vortex trapping due to pinning sites or surface barriers could result in delayed vortex relaxations showing a paramagnetic response. Such a PME peak, but of a much smaller magnitude, was observed in cuprates under fields of a few Oe [30].

C. Diode effect

Another interesting phenomenon observed in our films is the diode effect as presented in Figs. 7 and 8. The best way to observe this effect is via the voltage versus current curves (VICs) as depicted in Fig. 7 for a few temperatures. In general, a superconducting diode effect (SDE) can be observed in hysteretic (or nonreciprocal) superconductive Josephson junctions, where the supercurrents with increasing and decreasing bias currents are different $I_c^+ \neq |I_c^-|$. Then, when using a modulated bias current with amplitude in between these two supercurrents, the system will alternate between resistive and non-resistive states, which is the basic rectifying diode effect [17]. Here, in Fig. 7 (a) to (c) one can see *fully polarized* VICs, where on negative bias the films are resistive, while on positive bias they are superconducting. In (d), very close to T_c of zero resistance, the VIC is almost Ohmic all the way with only a tiny supercurrent part. We emphasize that there is almost no hysteresis in our case, and our SDE is more like the diode effect seen in semi-conductors but with a zero resistance in the more conductive branch. Theoretically, the SDE originates in materials with broken time-reversal and inversion symmetries [31–34]. Most of these studies assumed the presence of an external magnetic field, but some discussed also field-free SDE [17]. Internal Zeeman fields and disorder in nonreciprocal materials with strong spin-orbit or Rashba interactions, can also facilitate field-free SDE [32].

To our surprise, the observed SDE was easily polarity reversed as can be seen in Fig. 8 (a) to (c). This was found on the *same* film as in Fig. 7, but with newly prepared contacts with obviously a slightly different geometry. Mori et al. showed theoretically that by changing the distance between the superconducting electrodes, the SDE polarity could be reversed and that this effect is periodical in distance [18]. So in our case, the superconducting islands or domains can be considered as S-electrodes, and the black STO as the connecting normal metal (N-electrode) in the Mori et al. scenario. It should be noted that as long as there is no

perculative supercurrent in the nickelate film (between T_c onset and $T_c(R=0)$), the bias current will mostly flow via the highly conductive normal STO wafer, with occasional shunts through adjacent superconducting islands, as depicted in the schematic drawing of the inset to Fig. 6.

D. Supercurrents

Figures 7 and 8 were used to determine the supercurrents versus temperature in our film, as depicted in Fig. 8 (d). Due to the asymmetric VICs with different I_c^+ and $|I_c^-|$, we determined the combined supercurrents as $I_c^+ + |I_c^-|$. In the symmetric VIC case, it would amount to $2I_c$, while in the fully Asymmetric case (as in Fig. 7), it would be the standard I_c . We used a $\pm 2.5 \mu\text{V}$ criterion to asses the combined supercurrent. This criterion can be inferred from the noise of the VICs of Fig. 7 (a) and (b) at 1.8 K. The uninterrupted trace voltage noise is about $5 \mu\text{V}$ ($2\sigma_1$), while the occasional telegraph-jumps are about $7 \mu\text{V}$. Thus, the overall noise is about $12 \mu\text{V}$ ($2\sigma_2$). Disregarding the telegraph-noise which is less prevalent at higher temperatures, we end up with the $\sigma_1 = 2.5 \mu\text{V}$ criterion. Fig. 8 (d) shows that the supercurrent in our film decreases significantly at about 25-30 K, and is zero at 50 K. Therefore, much optimization work is needed to push the supercurrent to a higher temperature, closer to T_c onset at 50-70 K. Needless to say that identifying the mechanism responsible for this high T_c onset would help attain this goal. Finally, we stress again that the present high T_c results are different from those obtained in the well oxygenate $\text{La}_3\text{Ni}_2\text{O}_7$ phase [7, 13, 15, 16], in that our nickelate films are highly oxygen deficient and strongly affected by the highly reduced black STO substrate.

V. CONCLUSIONS

In this study, we demonstrated three noteworthy phenomena in oxygen-deficient nickelate thin films on highly reduced black STO substrates: A T_c onset enhancement to 50-70 K, a giant paramagnetic Meissner effect peak, and a highly asymmetric nonreciprocal superconductive diode effect. All of these results were obtained on highly reduced and highly conducting black STO substrates, which are essential for the present observations. The phase responsible for these effects is still the 112 infinite-layer phase, with admixture of higher oxygen content variants such as $11(2+\delta)$ with $0 < \delta < 1$. Further research is needed to identify the exact mechanism at the origin of these remarkable phenomena in nickelate films.

ACKNOWLEDGMENTS

We are grateful to A. Kanigel for useful discussions. We thank Yaron Kauffmann, Galit Atiya and Michael Kalina from the MIKA facility at the Technion for performing the STEM measurements.

SUPPLEMENT

A: XRD of the 80 and 30 nm thick films

Figure S1 (a) depicts XRD spectra of the NSNO2red6h film. Clearly, if there are any film peaks, they are within the noise level of this measurement, or affected by the strong (n00) peaks of the STO substrate. (b) shows a smaller XRD range near the (200) peak of the STO substrate, where results of the virgin films NSNO1 and NSNO2 together with the annealed film NSNO2red6h are plotted. Both virgin films before the annealing have prominent (002) peaks of the perovskite $Nd_{0.8}Sr_{0.2}NiO_3$ phase. After 6 h annealing in CaH_2 at 320°C of the NSNO2 film that produced the NSNO2red6h film, the (002) film peak almost disappeared and there is still no clear trace of any other film peaks besides those of the STO wafer. The "knee" at 48° is apparently due to remanence of the (002) film peak of the perovskite 113 phase.

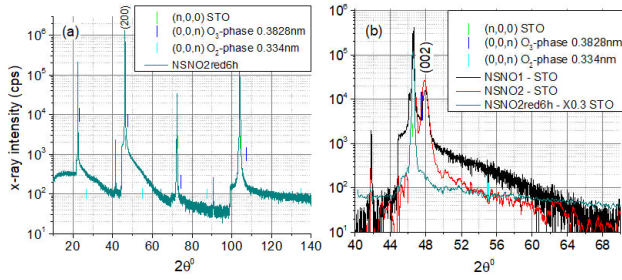


FIG. S1. (a) Full range XRD of the NSNO2red6h film. No apparent film peaks are seen here due to the polycrystalline nature of this film as shown in Fig. 4 (c) and (d), and the high noise level of the XRD system. (b) XRD of the NSNO1, NSNO2 and NSNO2red6h films near the (200) peak of the (100) STO wafer. The "knee" of the NSNO2red6h film at 48° originates in remanence of the (002) film peak of the perovskite phase.

B: M vs H of a bare STO wafer

Figure S2 shows the magnetic moment at 1.8 and at 100 K versus perpendicular magnetic field of a bare (100) STO wafer without a nickelate film and without annealing in CaH_2 . The field was cycled from 0 Oe to ± 5000 Oe and back to 0 Oe. The data sets were taken after ZFC. The saturation field of ~ 750 Oe at 1.8 K was reduced to ~ 550 Oe at 100 K. Clearly, the bare STO substrate is ferromagnetic, and the response at 1.8 K here is similar to that of the reduced NSNO1red1h sample of Fig. 2 (d) of the main article.

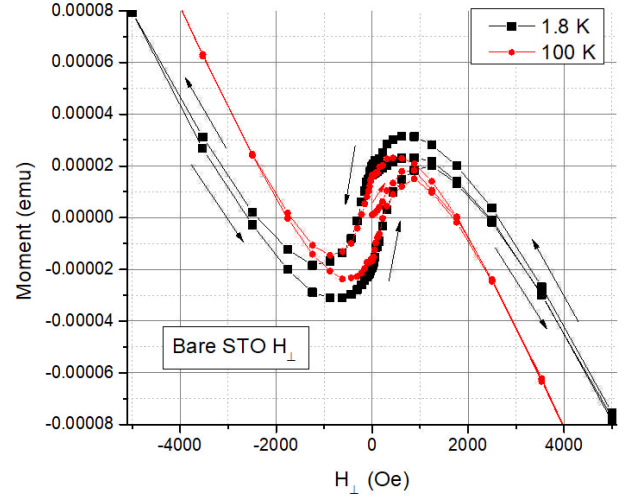


FIG. S2. Moment versus perpendicular magnetic field of a bare STO wafer at 1.8 and 100 K. The arrows show the magnetic field cycling sequence starting and ending at 0 Oe.

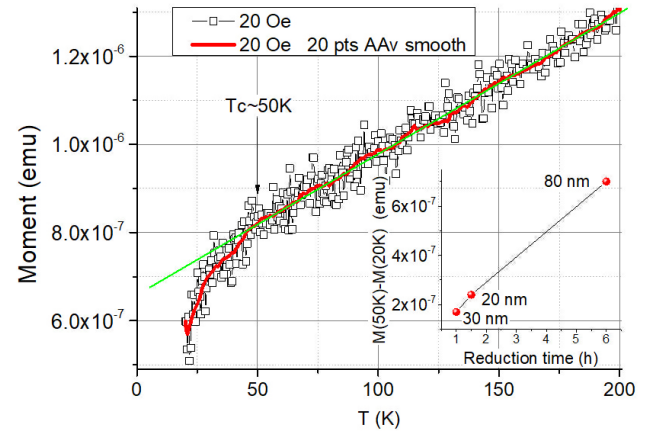
C: $T_c \sim 50$ K of a 20 nm thick film

FIG. S3. Moment versus temperature of a 20 nm thick NSNO3red1.5h film measured under 20 Oe field. This film was reduced for 1.5 h in CaH_2 at 320°C under pumping at $\sim 10^{-5}$ Torr. The measurement was carried out under heating from 20 K after field cycling to ± 5000 Oe at 1.8 K. The inset shows the net moments between 20 and 50 K of three films (NSNO1red1h, NSNO3red1.5h and NSNO2red6h of thicknesses 30, 20 and 80 nm, respectively) versus their reduction time.

In addition to the 30 and 80 nm thick films described in the main article, we also prepared films of 10 and 20 nm thickness. These films were not as extensively characterized, but here in Fig. S3 we present magnetization moment measurements versus temperature of a 20 nm thick film that was reduced for 1.5 h in CaH_2 at 320°C . One can see that the high-temperature transition at ~ 50 K

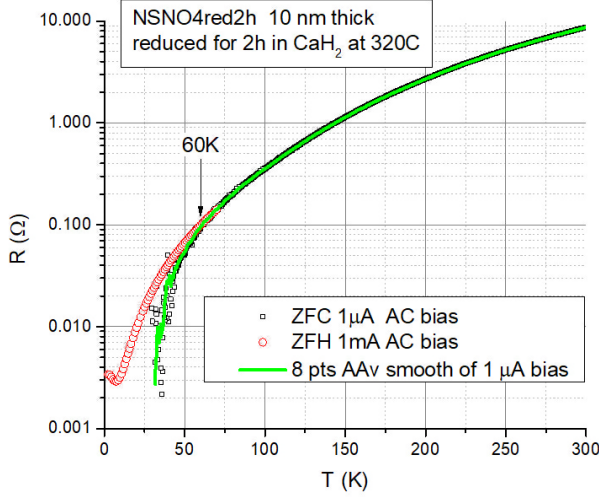


FIG. S4. R versus T of NSNO4red2h, a 10 nm thick film, as measured by the PPMS system at $1\ \mu\text{A}$ and $1\ \text{mA}$ bias. At low temperatures, the IVCs are linear only very close to zero bias due to the diode effect (see Figs. 7 and 8 of the main article). Therefore, the $1\ \text{mA}$ bias result at low temperatures is misleading and shows finite resistance below $30\ \text{K}$ (see a similar behavior when using the PPMS system in Fig. 6 of the main article). Therefore, the noisy data under $1\ \mu\text{A}$ bias at low temperatures is more reliable. It shows a transition onset (deviation from the $1\ \text{mA}$ bias result) already at about $60\ \text{K}$.

is well reproduced, supporting the notion of a robust superconducting transition at $50\ \text{K}$. The inset to this figure shows the net magnitude of the moments between 20 and

$50\ \text{K}$ of this film versus reduction time, as well as those of the main article. One can see that these net moments are almost linear in the duration of their reduction time and almost independent of the films' thicknesses in this range. This result indicates that it is most likely that the moments originate at the interface between these films and their substrates, regardless of their thickness down to $20\ \text{nm}$. Figure 4 of the next D section shows that this is true also down to $10\ \text{nm}$.

D: R vs T of a $10\ \text{nm}$ thick film

Though we do not have magnetic moment results on our $10\ \text{nm}$ thick film (NSNO4red2h, reduced in CaH_2 at 320°C for $2\ \text{h}$), we do have transport results on it. Figure S4 depicts two resistance versus temperature results under low and high bias currents as measured by the PPMS system. We measured many IVCs using this system on this film and found very nonlinear behaviors at low temperatures. Nevertheless, at very low bias the IVCs were almost linear, but quite noisy. Therefore, the noisy R vs T here at low T and $1\ \mu\text{A}$ bias, which we ignored at the beginning, is actually the more reliable result. If we consider the $1\ \text{mA}$ bias result, down to about $50\ \text{K}$, as a background mostly due to the black STO substrate, then any deviation from it marks the onset of a possible superconducting transition. One can see that such a deviation of the $1\ \mu\text{A}$ biased curve occurs at about $60\ \text{K}$. Without the data of the main article, we would have continue to ignore the results of Fig. S4 here, but this data actually further support the existence of a superconducting transition above $50\ \text{K}$ ($60\ \text{K}$ here), as was clearly demonstrated in the main article.

-
- [1] D. Li, K. Lee, B. Y. Wang, M. Osada, S. Crossley, L. R. H., Y. Cui, Y. Hikita, and H. Y. Hwang, Superconductivity in an infinite-layer nickelate, *Nature* **572**, 624 (2019).
 - [2] M. R. Norman, Entering the nickel age of superconductivity, *Physics* **13**, 85 (2020).
 - [3] D. Li, B. Y. Wang, K. Lee, S. P. Harvey, M. Osada, Goodge, B. H., L. F. Kourkoutis, and H. Y. Hwang, Superconducting dome in $\text{Nd}_{1-x}\text{Sr}_x\text{NiO}_2$ infinite layer films, *Phys. Rev. Lett.* **125**, 027001 (2020).
 - [4] M. Osada, B. Wang, B. Goodge, K. Lee, H. Yoon, D. Sakuma, K.; Li, M. Miura, L. Kourkoutis, and H. Hwang, A superconducting praseodymium nickelate with infinite layer structure, *Nano Lett.* **20**, 5735 (2020).
 - [5] Q. Li, C. He, J. Si, X. Zhu, Y. Zhang, and H. Wen, Absence of superconductivity in bulk $\text{Nd}_{0.8}\text{Sr}_{0.2}\text{NiO}_2$, *Commun. Mat.* **16**, 1 (2020).
 - [6] X. Zhou, Z. Feng, P. X. Qin, H. Yan, S. Hu, H. Guo, X. Wang, H. Wu, X. Zhang, and H. Y. Chen, Absence of superconductivity in $\text{Nd}_{0.8}\text{Sr}_{0.2}\text{NiO}_2$ thin films without chemical reduction, *Rare Met.* **39**, 368 (2020).
 - [7] G. Zhou, W. Lv, H. Wang, Z. Nie, Y. Chen, Y. Li, H. Huang, W. Chen, Y. Sun, Q.-K. Xue, and Z. Chen, Ambient-pressure superconductivity onset above $40\ \text{K}$ in bilayer nickelate ultrathin films, *arXiv* (2024).
 - [8] S. Zeng, C. Tang, X. Yin, C. Li, Z. Huang, J. Hu, W. Liu, G. Omar, H. Jani, and Z. Lim, Phase diagram and superconducting dome of infinite-layer $\text{Nd}_{0.8}\text{Sr}_{0.2}\text{NiO}_2$ thin films, *Phys. Rev. Lett.* **125**, 147003 (2020).
 - [9] Q. Gu, Y. Li, S. Wan, H. Li, W. Guo, H. Yang, Q. Li, X. Zhu, X. Pan, and Y. Nie, Two superconducting components with different symmetries in $\text{Nd}_{0.8}\text{Sr}_{0.2}\text{NiO}_2$ films, *Nat. Commun.* **11**, 6027 (2020).
 - [10] K. Lee, B. Y. Wang, M. Osada, B. H. Goodge, T. C. Wang, Y. Lee, S. Harvey, W. J. Kim, Y. Yu, C. Murthy, S. Raghu, L. F. Kourkoutis, and H. Y. Hwang, Linear-in-temperature resistivity for optimally superconducting $(\text{Nd}, \text{Sr})\text{NiO}_2$, *Nature* **619**, 288 (2023).
 - [11] Y. Lee, X. Wei, Y. Yu, L. Bhatt, K. Lee, B. H. Goodge, S. P. Harvey, B. Y. Wang, D. A. Muller, L. F. Kourkoutis, W.-S. Lee, S. Raghu, and H. Y. Hwang, Millimeter-scale freestanding superconducting infinite-layer nickelate membranes, *arXiv* (2024).
 - [12] S. L. E. Chow, Z. Luo, and A. Ariando, Bulk superconductivity near $40\ \text{K}$ in hole-

- doped SmNiO_2 at ambient pressure, *Nature*, <https://www.nature.com/articles/s41586-025-08893-4> (2025).
- [13] H. Sun, M. Huo, X. Hu, J. Li, Z. Liu, Y. Han, L. Tang, Z. Mao, P. Yang, B. Wang, J. Cheng, D.-X. Yao, G.-M. Zhang, and M. Wang, Signatures of superconductivity near 80 K in a nickelate under high pressure, *Nature* **621**, 493 (2023).
 - [14] P. Puphal, Y.-M. Wu, K. Fürsich, H. Lee, M. Pakdaman, J. A. N. Bruin, J. Nuss, Y. E. Suyolcu, P. A. van Aken, B. Keimer, M. Isobe, and M. Hepting, Topotactic transformation of single crystals: From perovskite to infinite-layer nickelates, *Sci. Adv.* **7**, eabl8091 (2021).
 - [15] E. K. Ko, Y. Yu, Y. Liu, L. Bhatt, J. Li, V. Thampy, C.-T. Kuo, B. Y. Wang, Y. Lee, K. Lee, J.-S. Lee, B. H. Goodge, D. A. Muller, and H. Y. Hwang, Signatures of ambient pressure superconductivity in thin film $\text{La}_3\text{Ni}_2\text{O}_7$, *Nature* (2024).
 - [16] Y. Liu, E. K. Ko, Y. Tarn, L. Bhatt, B. H. Goodge, D. A. Muller, S. Raghu, Y. Yu, and H. Y. Hwang, Superconductivity and normal-state transport in compressively strained $\text{La}_2\text{PrNi}_2\text{O}_7$ thin films, *arXiv* (2025).
 - [17] S. Qi, J. Ge, C. Ji, Y. Ai, G. Ma, Z. Wang, Z. Cui, Y. Liu, Z. Wang, and J. Wang, High-temperature field-free superconducting diode effect in high- T_c cuprates, *Nature Comm.* **16**, 531 (2025).
 - [18] M. Mori, W. Koshibae, and S. Maekawa, Towards optimization of the josephson diode effect, *arXiv* (2025).
 - [19] W. Braunisch, N. Knauf, G. Bauer, A. Kock, A. Becker, B. Freitag, A. Grutz, V. Kataev, S. Neuhausen, B. Roden, D. Khomskii, D. Wohlleben, J. Bock, and E. Preisler, Paramagnetic meissner effect in high-temperature superconductors, *Phys. Rev. B* **48**, 4030 (1993).
 - [20] J. Linder and A. V. Balatsky, Odd-frequency superconductivity, *Rev. Mod. Phys.* **91**, 045005 (2019).
 - [21] M. R. Koblishka, L. Pust, C.-S. Chang, T. Hauet, and A. Koblishka-Veneva, The paramagnetic meissner effect (pme) in metallic superconductors, *Metals* **13**, 1140 (2023).
 - [22] V. V. Moshchalkov, X. G. Qiu, and V. Bruyndoncx, Paramagnetic meissner effect from the self-consistent solution of the ginzburg-landau equations, *Phys. Rev. B* **55**, 11793 (1997).
 - [23] X. Lin, G. Bridoux, A. Gourgout, G. Seyfarth, S. Krämer, M. Nardone, B. Fauque, and K. Behnia, Critical doping for the onset of a two-band superconducting ground state in $\text{SrTiO}_{3-\delta}$, *Phys. Rev. Lett.* **112**, 207002 (2014).
 - [24] M. Rossi, H. Lu, K. Lee, B. H. Goodge, J. Choi, M. Osada, Y. Lee, D. Li, B. Y. Wang, D. Jost, S. Agrestini, M. Garcia-Fernandez, Z. X. Shen, K. J. Zhou, E. Been, B. Moritz, L. F. Kourkoutis, T. P. Devereaux, H. Y. Hwang, and W. S. Lee, Universal orbital and magnetic structures in infinite-layer nickelates, *Physical Review B* **109**, 024512 (2024).
 - [25] C. T. Parzyck, A. G. Gianfrancesco, T. Schumann, M. E. Holtz, K. N. Luckyanova, D. Su, D. G. Schlom, and L. F. Kourkoutis, Absence of $3a_0$ charge density wave order in the infinite-layer nickelate NdNiO_2 , *Nature Materials* **23**, 486 (2024).
 - [26] A. O. Raji, X. Li, and Y. Yang, Charge distribution across capped and uncapped infinite-layer neodymium nickelate thin films, *Small* **19**, 2304872 (2023).
 - [27] G. Koren, A. Eyal, L. Iomin, and Y. Nitzav, Observation of josephson-like tunneling junction characteristics and positive magnetoresistance in oxygen deficient nickelate films of $\text{Nd}_{0.8}\text{Sr}_{0.2}\text{NiO}_{3-\delta}$, *Materials* **14**, 7689 (2021).
 - [28] G. Koren, A. Gupta, R. J. Baseman, M. I. Lutwyche, and R. B. Leibowitz, Laser wavelength dependent properties of $\text{YBa}_2\text{Cu}_3\text{O}_{7-\delta}$ thin films deposited by laser ablation, *Appl. Phys. Lett.* **55**, 2450 (1989).
 - [29] H. Yamada and G. R. Miller, Point defects in reduced strontium titanate, *Jour. Solid State Chem.* **6**, 169 (1973).
 - [30] S. Riedling, G. Bräuchle, R. Lucht, K. Röhberg, H. v. Löhneysen, H. Claus, A. Erb, and G. Müller-Vogt, Observation of the wohlleben effect in $\text{YBa}_2\text{Cu}_3\text{O}_{7-\delta}$ single crystals, *Phys. Rev. B* **49**, 13283 (1994).
 - [31] J. J. He, Y. Tanaka, and N. Nagaosa, A phenomenological theory of superconductor diodes, *New J. Phys.* **24**, 053014 (2022).
 - [32] S. Ilić and F. S. Bergeret, Theory of the supercurrent diode effect in rashba superconductors with arbitrary disorder, *Phys. Rev. Lett.* **128**, 177001 (2022).
 - [33] N. F. Q. Yuan and L. Fu, Supercurrent diode effect and finite-momentum, *PNAS* **119**, e2119548119 (2022).
 - [34] F. Ando, Y. Miyasaka, T. Li, J. Ishizuka, T. Arakawa, Y. Shiota, T. Moriyama, Y. Yanase, and T. Ono, Observation of superconducting diode effect, *Nature* **584**, 373 (2022).